HAL open science

Assessment of SCARDEC source parameters of global large (Mw $\geq$ 7.5) subduction earthquakes

K. Lentas, Ferreira M. G. A., Martin Vallée

To cite this version:

K. Lentas, Ferreira M. G. A., Martin Vallée. Assessment of SCARDEC source parameters of global large (Mw $\geq$ 7.5) subduction earthquakes. Geophysical Journal International, 2013, 195 (3), pp.1989 - 2004. 10.1093/gji/ggt364 . hal-01856004

HAL Id: hal-01856004

https://hal.science/hal-01856004

Submitted on 14 Oct 2021

HAL is a multi-disciplinary open access archive for the deposit and dissemination of scientific research documents, whether they are published or not. The documents may come from teaching and research institutions in France or abroad, or from public or private research centers.

L'archive ouverte pluridisciplinaire **HAL**, est destinée au dépôt et à la diffusion de documents scientifiques de niveau recherche, publiés ou non, émanant des établissements d'enseignement et de recherche français ou étrangers, des laboratoires publics ou privés.

Distributed under a Creative Commons Attribution 4.0 International License

Geophysical Journal International

Geophys. J. Int. (2013) **195,** 1989–2004
Advance Access publication 2013 October 3

doi: 10.1093/gji/ggt364

Assessment of SCARDEC source parameters of global large ($M_w \geq 7.5$) subduction earthquakes

K. Lentas,[1] A. M. G. Ferreira[1,2,*] and M. Vallée[3,†]

[1] *School of Environmental Sciences, University of East Anglia, Norwich, NR4 7TJ, UK. E-mail: K.Lentas@uea.ac.uk*
[2] *ICIST, Instituto Superior Técnico, Technical University of Lisbon, Lisbon, Portugal*
[3] *Géoazur, Université de Nice Sophia Antipolis, IRD-CNRS-OCA, Valbonne, France*

Accepted 2013 September 9. Received 2013 September 6; in original form 2012 October 3

Downloaded from https://academic.oup.com/gji/article/195/3/1989/627339 by guest on 14 October 2021

SUMMARY

Rapid and accurate source characterizations of large, shallow subduction earthquakes are key for improved tsunami warning efforts. We assess the quality of source parameters of large magnitude ($M_w \geq 7.5$) shallow subduction earthquakes of the past 20 yr determined using SCARDEC, a recent fully automated broad-band body-wave source inversion technique for the fast estimation of the moment magnitude, depth, focal mechanism and source time functions of global events. We find that SCARDEC source parameters agree well with those reported in the global centroid moment tensor (GCMT) catalogue, with only the fault dip angle showing a tendency for steeper SCARDEC dip values than GCMT. We investigate this discrepancy through independent validation tests of the source models by: (i) testing how well they explain data not used in their construction, notably low-frequency normal mode data; and, (ii) assessing the data fit using 3-D forward modelling tools more sophisticated than those used to build the source models; specifically, we use a spectral element method for a 3-D earth model. We find that SCARDEC source parameters explain normal mode data reasonably well compared to GCMT solutions. In addition, for the 3-D earth model used in our experiments, SCARDEC dip angles explain body-wave data similarly or slightly better than GCMT. Moreover, SCARDEC dip angles agree well with results from individual earthquake studies in the literature and with geophysical constraints for different subduction zones. Our results show that SCARDEC is a reliable technique for rapid determinations of source parameters of large ($M_w \geq 7.5$) subduction earthquakes. Since the SCARDEC method provides realistic source time functions allowing the fast identification of long-duration tsunami earthquakes, it is complementary to existing methods routinely used for earthquake monitoring and suitable for ocean-wide tsunami warning purposes.

Key words: Earthquake source observations; Body waves; Surface waves and free oscillations.

1 INTRODUCTION

Fast, automated and reliable earthquake source parameter determinations are of critical importance for rapid seismic hazard assessment and relief response efforts. In particular, accurate estimates of subduction earthquake moment magnitude, depth, fault dip angle and source time functions give useful input information for effective tsunami warning systems. Earthquake source parameters are routinely determined and reported in global catalogues, such as the global centroid moment tensor (GCMT) catalogue (http://www.globalcmt.org/CMTsearch.html), and the U.S. Geological Survey—National Earthquake Information Center (USGS—NEIC, http://earthquake.usgs.gov/earthquakes/recenteqsww/). For large magnitude ($M_w \geq 7.5$) earthquakes, the GCMT method (e.g. Dziewonski *et al.* 1981; Ekström *et al.* 2012) often uses only long-period mantle waves ($T \sim 125$–350 s), and in some cases employs long-period body waves ($T \sim 40$–150 s) as well as mantle and surface wave ($T \sim 50$–150 s) data. On the other hand, the USGS catalogue reports, among others, source models obtained using W-phase data (Kanamori & Rivera 2008; Hayes *et al.* 2009; Duputel *et al.* 2012b). While surface waves are not ideal for rapid source parameter estimations, as they travel slower than body waves, the W-phase

*Now at: Department of Earth Sciences, University College London, London, UK.
†Now at: Institut de Physique du Globe de Paris, Université Paris Diderot, CNRS, Paris, France.

© The Authors 2013. Published by Oxford University Press on behalf of The Royal Astronomical Society.

travels faster than shear waves, thus being more suitable for real time applications, notably for tsunami alert purposes (Kanamori & Rivera 2008). However, for shallow dip-slip earthquakes, which often occur in subduction zones, both W-phase and GCMT methods suffer from a trade-off between the seismic moment and the dip angle (Kanamori & Given 1981; Tsai *et al.* 2011) when Rayleigh waves are used. For these earthquakes, the excitation of long-period surface waves is proportional to both the seismic moment and the sine of the dip angle ($M_0 \sin 2\delta$), but the two parameters are not well constrained separately.

Body-wave techniques can help address these issues, as broadband body waves used in earthquake source inversions, typically with wave periods smaller than those of surface waves, are little affected by the moment-dip trade-off, which only becomes significant for earthquakes very close to the surface (see, e.g. the radiation pattern terms for the P-pP-sP wavetrain in Bouchon 1976, and Figs S1–S4 and corresponding accompanying text). An example of such body-wave technique is the recently developed SCARDEC method (Vallée *et al.* 2011), which is now fully automated and used in rapid routine analyses of large ($M_w \geq 5.5$–6.0) global earthquakes available online (http://geoazur.oca.eu/SCARDEC) about 45 min after an event. The method uses a deconvolution approach to determine the optimal set of source parameters. Ray theory is used to calculate double couple point-source body-wave signals in the 1-D IASP91 earth model (Kennett & Engdahl 1991), for a given source depth, fault geometry and mechanism (strike, dip and rake). By deconvolving these point source signals from real data, and taking into account some physical constraints on the resulting relative source time functions (see Vallée *et al.* 2011, for details), the SCARDEC method retrieves the optimal set of source parameters. SCARDEC thus determines simultaneously relative source time functions at each station, along with the focal mechanism, depth and moment magnitude. The determination of relative source time functions, which are allowed to be different at each station, makes SCARDEC particularly well adapted to the analysis of large earthquakes, setting it apart from classical body-wave approaches (e.g. Nabelek 1984). Moreover, unlike many other routine earthquake source analysis techniques and studies in the literature, the SCARDEC method reports uncertainties in earthquake magnitude, dip angle and depth. As explained in Vallée *et al.* (2011), a heuristic approach is used to estimate uncertainties, whereby fixing the fault's strike and rake to their optimal values, misfit values are computed for a range of 30 km around the optimal source depth and for a range of $\pm 15^\circ$ around the optimal dip angle. The analysis of the misfit functions obtained following this procedure for a large number of earthquakes showed that the misfit function has a typical bell-shape, with a flat misfit area surrounded by a zone of rapidly increasing misfit. The limit of the flat misfit area was found to be controlled by a 10 per cent misfit deterioration criterion, which corresponds to the extreme acceptable models. While these uncertainty estimates do not arise from a rigorous statistical analysis, they reflect the resolution of the SCARDEC method, being more realistic than, for example the standard errors reported in the GCMT catalogue, which assume that uncorrelated noise is the only source of error, leading to very low uncertainty values, particularly for large events (see, e.g. the discussion in Hjörleifsdóttir & Ekström 2010; Duputel *et al.* 2012a).

As mentioned above, the SCARDEC method is now a fully automated technique which analyses earthquakes with $M_w \geq 5.5$ in the NEIC catalogue. It uses only up to a 32 min interval of data after the event's origin, and the inversions take 5–12 min, so that SCARDEC solutions are obtained within 45 min after the earthquake. Vallée *et al.* (2011) give a full description of the method and they show results obtained from 17 large ($M_w \geq 7.8$) subduction earthquakes of the past 20 yr. The limited magnitude range in their study is related with the frequency range of the data used in those inversions. In the newer, refined version of the method which we assess in this paper, the high-pass period depends on the earthquake magnitude and duration, and ranges from 80 s for a $M_w \sim 6$ earthquake to 333 s for a very large and long source duration (SD) earthquake ($M_w \sim 9$). Specifically, the choice of the optimal high-pass filter (HPF) represents a balance between three factors: (i) the corner frequency of the earthquake, which is related to its SD; (ii) the signal-to-noise ratio and (iii) the validity of the body-wave formalism used in the SCARDEC method. For the large earthquakes analysed in this study, using a HPF of 0.005 Hz always respects condition (ii). However, when the earthquakes have very long SDs, their corner frequency (which is roughly close to the inverse of the SD) may be too close to 0.005 Hz, which lead us to lower the HPF to a value equal to 1/(2.5 SD). It must be noted that this can be done because the first step of the SCARDEC technique is to determine the SD by a high-frequency analysis of the *P* waves. Finally, condition (iii) imposes a lower bound to the HPF, as very low-frequency waves, such as the W-phase (Kanamori & Rivera 2008), are not considered in the SCARDEC formalism. This explains why the HPF is not chosen to be lower than 0.003 Hz. This implementation leads to slightly different results to those presented by Vallée *et al.* (2011). Updated source parameters and their acceptable intervals are shown in Table S1, which shows that for the 17 earthquakes common to the two studies, there are some slight differences. For example, the updated moment magnitude values in this study are slightly larger than those reported by Vallée *et al.* (2011, with a median difference in M_w of about 0.05). This slight increase in moment magnitude naturally results from lowering the HPF as explained above for earthquakes with a SD longer than 80 s. Details on the updated results, stations used and optimal source model—data fit plots can be found at http://geoazur.oca.eu/SCARDEC . Hereinafter, we will refer to Vallée *et al.* (2011) as the source for the SCARDEC technique, but we will refer to Table S1 for the SCARDEC source parameters used in this study. Even if varying little from the SCARDEC solutions reported by Vallée *et al.* (2011), given the refinement of the technique to account for the effect of the earthquake's corner frequency in a more rigorous way, the latest SCARDEC solutions should be the most reliable.

In this study, we carry out independent validation tests to objectively assess the quality and robustness of the updated SCARDEC source models. We focus on 34 subduction earthquakes with $M_w \geq 7.5$, occurring at shallow depths, which can potentially excite tsunamis with significant heights, depending also on the fault dip angles. The choice of our moment magnitude criterion is motivated by existing tsunami alert systems, such as the Pacific Tsunami Warning Centre (PTWC), which issues tsunami messages for earthquakes of the same or higher moment magnitudes (http://ptwc.weather.gov/ptwc/about_messages.php). We analyse large shallow earthquakes that occurred in the past 20 yr and we carry out comparisons with solutions in the GCMT catalogue, as it is the most widely used and complete global moment tensor catalogue for that period. We start by testing how well SCARDEC source parameters explain data not used to constrain them; specifically, we use low-frequency normal mode data. As the source parameters are based on simplifying approaches such as 1-D Earth ray theory for the SCARDEC method (Vallée *et al.* 2011), and the great-circle approximation for the GCMT method (Dziewonski *et al.* 1981), we then assess the impact of such simplifications by using a more sophisticated technique—the spectral element method (SEM) on a

Downloaded from https://academic.oup.com/gji/article/195/3/1989/627339 by guest on 14 October 2021

3-D earth model (Komatitsch & Tromp 1999)—to verify how well the source models explain body-wave data. Finally, we compare the various dip angle estimates with those from previous individual earthquake studies and with geophysical constraints on subduction zones, and discuss the implications of this work in terms of the reliability of the SCARDEC method for routine subduction earthquake characterizations and ocean-wide tsunami warning purposes.

More broadly, this study contributes to ongoing efforts in earthquake source model validation (e.g. the source inversion validation project, http://eqsource.webfactional.com/wiki/). Finding objective strategies to benchmark, compare and independently test the quality of earthquake source models, as done in this study, is a crucial step for the rigorous quantification of seismic source processes and associated uncertainties in future earthquake studies.

2 SUBDUCTION EARTHQUAKES STUDIED

We first consider all the large ($M_w \geq 7.5$), shallow (depth ≤ 50 km), interplate subduction (thrust mechanism with a dip angle smaller than 40°) earthquakes that occurred in the past 20 yr. We exclude the 2004 great Sumatra earthquake whose exceptionally long SD causes poor results when using the SCARDEC method. Moreover, we exclude large events occurring minutes to a day after a major earthquake (e.g. the 2000 November 17 New Britain earthquake and the large early aftershock of the 2011 Tohoku-Oki earthquake), whose interference causes noisy waveforms. This leads to a selection of the 34 earthquakes shown in Fig. 1 and Table 1. Their SCARDEC source parameters, including uncertainties in dip angle, depth and magnitude can be found in Table S1.

Fig. 2 compares GCMT and SCARDEC earthquake source parameters for the studied earthquakes. There is generally a good agreement between SCARDEC and GCMT for fault strike, rake, depth and M_w, especially when taking SCARDEC uncertainties into account (i.e. often the range of acceptable SCARDEC source parameters comprises the GCMT solution), with no obvious trends in the scatter plots for these parameters. If realistic errors of fault geometry and mechanism were reported by GCMT, there might be even more considerable overlap between error bars. In contrast, SCARDEC dip angles are generally steeper than those in the GCMT

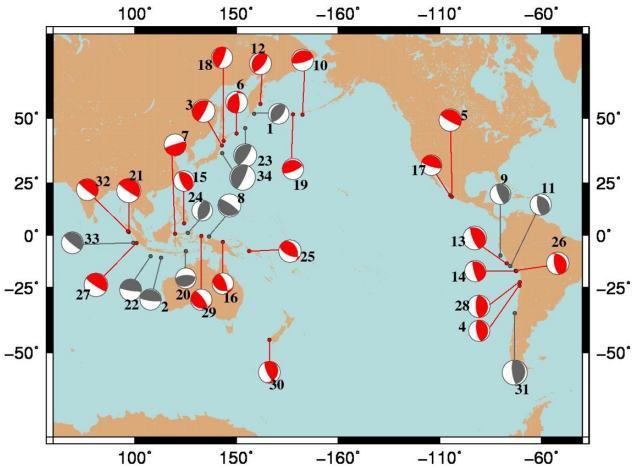

Figure 1. Global map showing the locations and GCMT source mechanisms of the major subduction earthquakes considered in this study. Earthquakes where GCMT dip angles lay outside of SCARDEC dip angle intervals are plotted in red. All the remaining earthquakes are plotted in grey. A detailed list of the earthquakes can be found in Table 1 and in Table S1.

Table 1. List and index codes of the large magnitude ($M_w \geq 7.5$) shallow subduction earthquakes of the past 20 yr used in this study. Their GCMT and SCARDEC fault geometries are shown by their beach balls. Earthquakes where GCMT dip angles lay outside of SCARDEC dip angle intervals are shown in bold (earthquakes in red in Figs 1–3).

Index	Event name	GCMT	SCARDEC
1	060893D - Kamchatka 1993		
2	060294A - Java 1994		
3	**122894C - Honshu 1994**		
4	**073095A - Chile 1995**		
5	**100995C - Jalisco 1995**		
6	**120395E - Kuril 1995**		
7	**010196C - Minahassa 1996**		
8	021796B - Irian Jaya 1996		
9	022196B - N. Peru 1996		
10	**061096B - Andreanof 1996**		
11	111296D - Peru 1996		
12	**120597C - Kamchatka 1997**		
13	**062301E - Peru 2001a**		
14	**070701F - Peru 2001b**		
15	**030502H - Mindanao 2002**		
16	**090802H - New Guinea 2002**		
17	**012203A - Jalisco 2003**		
18	**092503C - Hokkaido 2003**		
19	**111703B - Rat Islands 2003**		
20	111104M - Timor 2004		
21	**200503281609A - Sumatra 2005**		
22	200607170819A - Java 2006		

Downloaded from https://academic.oup.com/gji/article/195/3/1989/627339 by guest on 14 October 2021

Table 1 (*Continued*)

Index	Event name	GCMT	SCARDEC
23	200611151114A - Kuril 2006		
24	200701211127A - Molucca 2007		
25	**200704012039A - Solomon Islands 2007**		
26	**200708152340A - Peru 2007**		
27	**200709121110A - Sumatra 2007**		
28	**200711141540A - Chile 2007**		
29	**200901031943A - Irian Jaya 2009**		
30	**200907150922A - New Zealand 2009**		
31	201002270634A - Chile 2010		
32	**201004062215A - N. Sumatra 2010**		
33	201010251442A - S. Sumatra 2010		
34	201103110546A - Honshu 2011		

catalogue, showing a clear systematic trend of larger SCARDEC dip angles, except for six events (Peru 1996, Kamchatka 1997, Timor 2004, Kuril 2006, Solomon Islands 2007, Peru 2007; see Tables 1 and S1 for further details about these earthquakes and corresponding source parameters). The average difference in dip angles between SCARDEC and GCMT ($\Delta\delta = \delta^{\mathrm{GCMT}} - \delta^{\mathrm{SCARDEC}}$) is $\bar{\Delta}\delta = -3.9^{\circ}$, with Jalisco 2003 having the largest dip angle difference ($\Delta\delta = -12.5^{\circ}$), and with 19 earthquakes showing dip angle differences larger than the average of differences. For the remaining earthquakes, while the trend in the differences between SCARDEC and GCMT dip angles generally persists, the differences are smaller, especially when taking into account the SCARDEC uncertainties.

Vallée *et al.* (2011) found that for half of the earthquakes in their study, steeper SCARDEC dip angle estimates were associated with a smaller moment magnitude than GCMT, with an average difference in M_{w} over all the earthquakes of 0.095. They showed that the discrepancies between GCMT and SCARDEC are consistent with the $M_{\mathrm{w}} - \delta$ trade-off, by using a corrected moment magnitude for GCMT, which lead to a lower average difference. In this study, we find a substantially lower average difference in magnitude between GCMT and the updated SCARDEC source parameters for the new set of earthquakes [0.00 for the whole set of earthquakes and 0.01 for the $M_{\mathrm{w}} \geq 7.8$ earthquakes studied by Vallée *et al.* (2011)]. The reasons and implications of these differences are discussed below in Section 6.

Fig. 3 compares SCARDEC and GCMT moment tensor components for the 34 earthquakes considered. Given that the dip angles show the largest discrepancies of all parameters in Fig. 2, this leads to the dip-slip components of the moment tensor ($M_{r\theta}$, $M_{r\phi}$) having the largest average differences between SCARDEC and GCMT among all the moment tensor component estimates.

In the remainder of this paper, we shall carry out independent tests of SCARDEC source models. Since the main differences between SCARDEC and GCMT source parameters are found for fault dip angles, we focus on the set of 22 earthquakes for which GCMT dip angles lay outside of SCARDEC dip angle intervals (see the red symbols in Figs 1–3 and the earthquakes in bold in Table 1).

3 NORMAL MODE DATA TESTS

Normal mode data illuminate overall bulk earthquake source characteristics and are a useful tool to test the SCARDEC method independently, as they are not used in the construction of SCARDEC source models. Moreover, the frequency range (0.1–4 mHz) of the very long time-series (48 hr) used in this test is much lower than that used in the shorter duration (25 min) surface wave comparisons (150–200 s) presented in Vallée *et al.* (2011). In order to study the Earth's normal modes, we use three-component broad-band data from the global seismographic network (GSN) for the earthquakes in this study.

In this section, we focus only on earthquakes with $M_{\mathrm{w}} \geq 7.8$, of the 22 earthquakes where GCMT dip angles lay outside of SCARDEC dip angle intervals. This magnitude threshold is used because only such large earthquakes can excite relatively well ultra-long-period normal modes (0.1–1.0 mHz), providing a high signal-to-noise ratio in this frequency range. The amplitude spectra of lower magnitude earthquakes is generally dominated by noise in this frequency range. This leads to a set of 14 earthquakes (Chile 1995, Jalisco 1995, Kuril 1995, Minahassa 1996, Andreanof 1996, Kamchatka 1997, Peru 2001, Hokkaido 2003, Sumatra 2005, Solomon Islands 2007, Peru 2007, Sumatra 2007, New Zealand 2009 and Sumatra 2010; see Tables 1 and S1 for details). We apply a fast Fourier transform (FFT) to 48 hr of continuous displacement data, after multiplication by a Hanning window, to obtain amplitude data spectra between 0.1 and 4.0 mHz. We visually examine all the amplitude spectra and only consider data in frequency intervals with high quality, similar to that shown in Fig. 4. We then calculate theoretical seismograms using a mode summation technique (e.g. Gilbert & Dziewonski 1975), for both the SCARDEC and GCMT source parameters. We sum over all the spheroidal and toroidal fundamental modes and overtones from 3233 s (${}_0S_2$) down to 30 s for completeness, for a spherically symmetric, non-rotating, elastic, isotropic (SNREI) earth model, using the 1-D PREM (Dziewonski & Anderson 1981) model. Since we use only 48 hr of data, we are not very sensitive to the splitting of low-frequency modes, and hence, for the purpose of comparing how well the two sets of source parameters fit the data, we do not take into account the effects of ellipticity and rotation in our calculations. The same processing as for the real data is then applied to the synthetics to obtain synthetic amplitude spectra. Despite calculating theoretical seismograms with periods down to 30 s, we compute amplitude spectra between 0.1 and 4.0 mHz (as for the real data).

We quantify the fit between synthetic and real data spectra by calculating L_2-norm amplitude misfits (eq. 1) and L_2-norm FFT real and imaginary part misfits (eq. 2):

$$m^2_{\mathrm{ampl.}} = \frac{\sum_i \sum_n [d_i^{\mathrm{A}}(f_n) - s_i^{\mathrm{A}}(f_n)]^2}{\sum_i \sum_n [d_i^{\mathrm{A}}(f_n)]^2} \quad (1)$$

Downloaded from https://academic.oup.com/gji/article/195/3/1989/627339 by guest on 14 October 2021

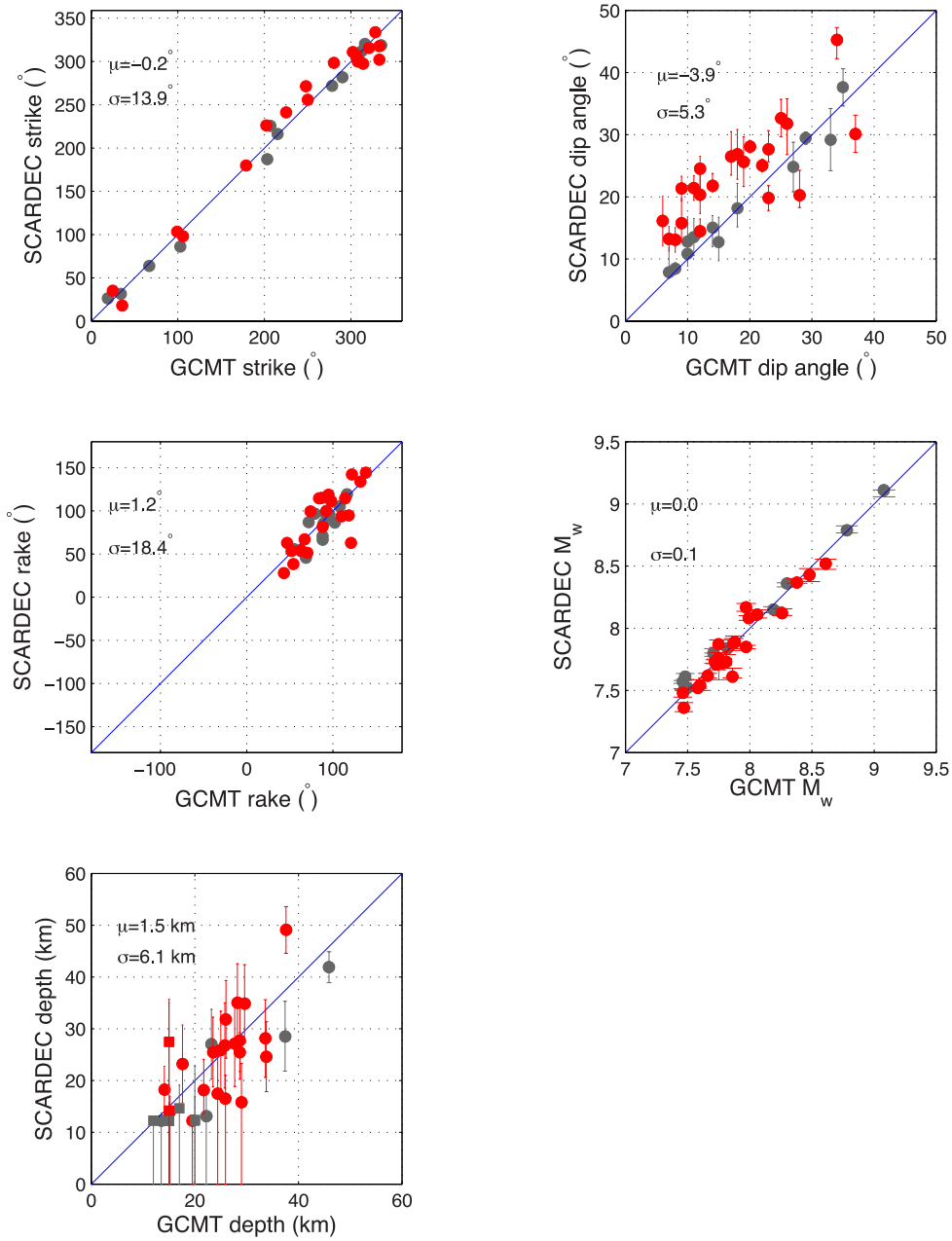

Figure 2. Scatter plots of GCMT source parameters versus SCARDEC (strike, dip, rake angles, depth and moment magnitude). Error bars correspond to SCARDEC uncertainties. Red circles correspond to the earthquakes studied, for which GCMT dip angles lay outside of SCARDEC dip angle intervals. Square symbols in the diagram with depth comparisons correspond to earthquakes where the GCMT depth is fixed. All the remaining earthquakes are plotted in grey. A detailed list of the earthquakes can be found in Table 1. Mean value (μ) and standard deviation (σ) of the differences between GCMT and SCARDEC parameters are plotted in the top left-hand side corner of each diagram.

$$m^2_{\mathrm{Re/Im}} = \frac{\sum_i \sum_n \{[d_i^{\mathrm{Re}}(f_n) - s_i^{\mathrm{Re}}(f_n)]^2 + [d_i^{\mathrm{Im}}(f_n) - s_i^{\mathrm{Im}}(f_n)]^2\}}{\sum_i \sum_n \{[d_i^{\mathrm{Re}}(f_n)]^2 + [d_i^{\mathrm{Im}}(f_n)]^2\}} \qquad (2)$$

where f_n is the nth frequency in the spectral domain, and d_i^A and s_i^{A} are the data and synthetic amplitude spectra at the ith station, respectively. d_i^{Re} and s_i^{Re}, and d_i^{Im} and s_i^{Im} are the real and imaginary parts of the data and synthetics in the frequency domain, respectively. The amplitude misfit evaluates the discrepancy in the amplitude spectra between the data and the synthetics, while the real and imaginary FFT part misfit provides information about the discrepancies in both the amplitude and phase of the signal. Noisy parts of the observed spectra are discarded from the misfit calculations.

An illustrative example of normal mode amplitude spectra comparisons can be found in Fig. 4 for the M_{w} 8.4 Sumatra 2007 earthquake. The earthquake occurred about 130 km SW of Bengkulu, with a rupture extending 350 km to the NW from the hypocentre and a duration of about 100 s (Konca *et al.* 2008). The main shock was followed by a moderate tsunami with respect to its magnitude, with run-up heights up to 4 m (Lorito *et al.* 2008; Borrero *et al.* 2009). Fig. 4 shows that GCMT and SCARDEC synthetics fit the observed normal mode amplitude spectra equally well, for both vertical and transverse component data. We calculated

Downloaded from https://academic.oup.com/gji/article/195/3/1989/627339 by guest on 14 October 2021

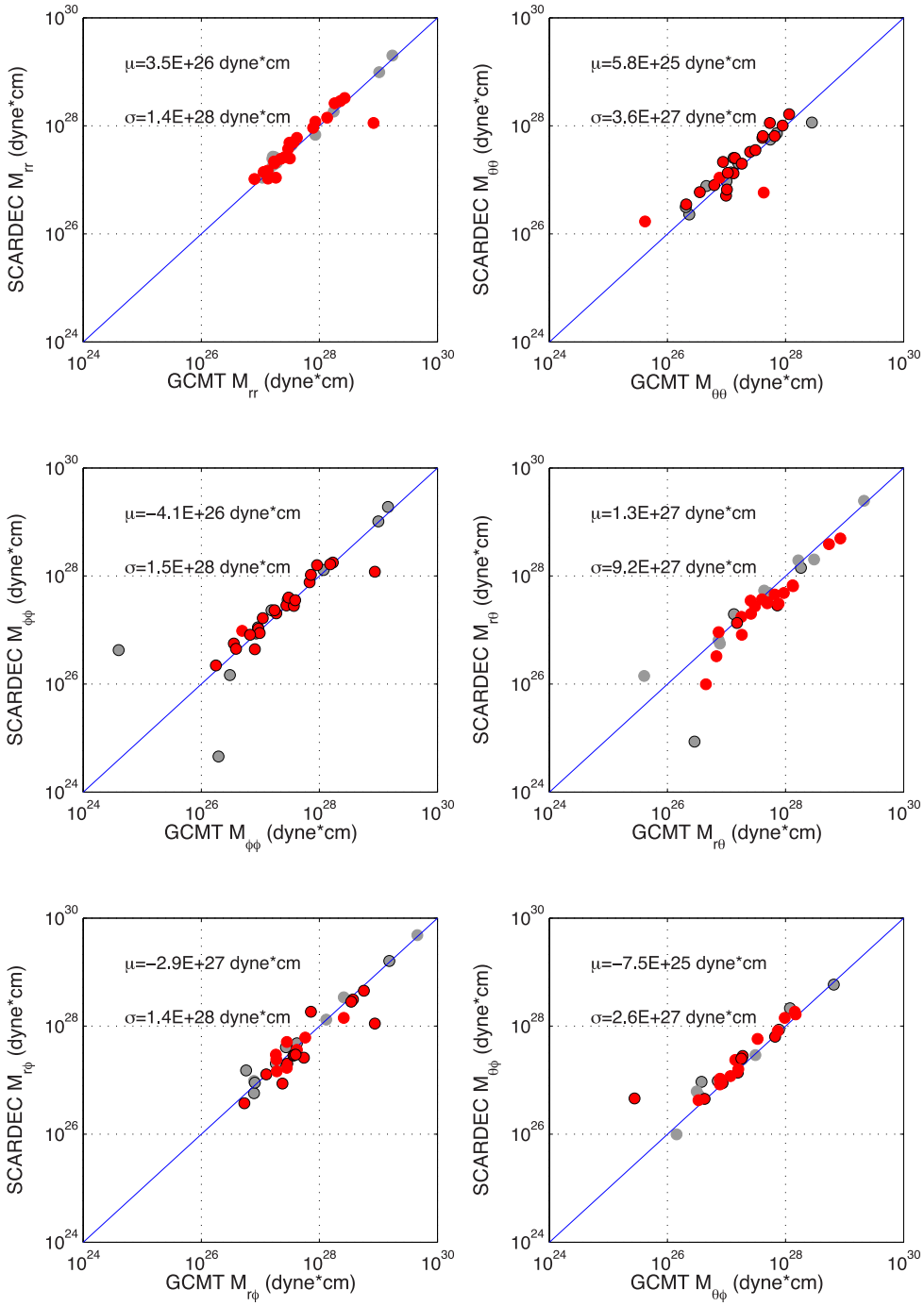

Figure 3. Scatter plots of GCMT moment tensor components versus SCARDEC. Red circles correspond to the earthquakes studied for which the GCMT and SCARDEC dip angles lay outside of SCARDEC dip angle intervals. All the remaining earthquakes are plotted in grey. Black circle contours indicate negative moment tensor components (all SCARDEC and GCMT moment tensor components compared here have the same signs). Mean value (μ) and standard deviation (σ) of the differences between GCMT and SCARDEC are indicated in the top left-hand side corner of each diagram.

amplitude misfits over 20 vertical and 13 transverse component traces and found the same results. Amplitude and real and imaginary part FFT misfits for GCMT are $m^2_{\mathrm{ampl.Z}} = 0.38$, $m^2_{\mathrm{Re/Im_Z}} = 0.90$, $m^2_{\mathrm{ampl.T}} = 0.52$ and $m^2_{\mathrm{Re/Im_T}} = 1.03$ for the vertical and transverse components, respectively. Misfit values for SCARDEC are $m^2_{\mathrm{ampl.Z}} = 0.38$, $m^2_{\mathrm{Re/Im_Z}} = 0.93$, $m^2_{\mathrm{ampl.T}} = 0.53$ and $m^2_{\mathrm{Re/Im_T}} = 1.06$, respectively.

Fig. 5 shows amplitude and Re/Im normal mode data misfits for the 14 earthquakes considered in this section. The differences between GCMT and SCARDEC misfit values are relatively small, with only the 1995 Jalisco earthquake showing a larger SCARDEC Re/Im misfit due to the combination of considerable differences in fault strike (8°), dip (12°) and M_{w} (0.13) between SCARDEC and GCMT source parameters. In most other cases, the GCMT misfit values are slightly lower than for SCARDEC, probably because the GCMT method uses hours of long-period mantle waves (with $T \sim 150$ s or longer), which are closer to the normal mode data used here, than the body-wave data used by SCARDEC. Overall,

Downloaded from https://academic.oup.com/gji/article/195/3/1989/627339 by guest on 14 October 2021

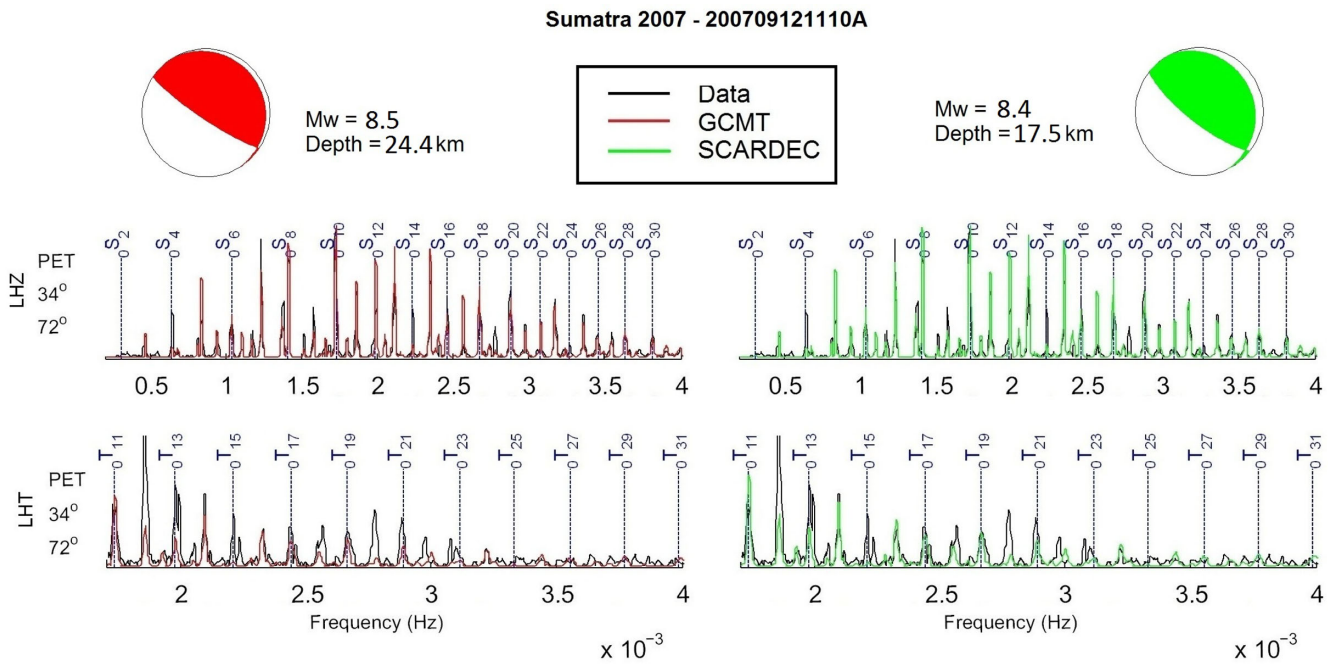

Figure 4. An illustrative example of vertical and transverse component normal mode spectra up to 4 mHz, calculated for the M_w 8.5 Sumatra 2007 earthquake with GCMT code 200709121110A, for GSN station PET. 48-hr data spectra are in black, GCMT synthetics in red and SCARDEC synthetics in green. PREM mode eigenfrequencies are shown in blue every two modes for clarity. All the noisy parts of the spectra are discarded from the plots and the misfit calculations. Station name, azimuth and epicentral distance are shown in the left-hand side from the top to the bottom. Amplitude misfits for vertical and transverse components over the total number of stations used (20 for the vertical and 13 for the transverse component) are: $m^2_{\mathrm{ampl.Z}} = 0.38$ and $m^2_{\mathrm{ampl.T}} = 0.52$ for GCMT, and $m^2_{\mathrm{ampl.Z}} = 0.38$ and $m^2_{\mathrm{ampl.T}} = 0.53$ for SCARDEC, respectively. Real and imaginary part FFT misfits are: $m^2_{\mathrm{Re/Im_Z}} = 0.90$, $m^2_{\mathrm{Re/Im_T}} = 1.03$ for GCMT and $m^2_{\mathrm{Re/Im_Z}} = 0.93$, $m^2_{\mathrm{Re/Im_T}} = 1.06$, for SCARDEC. Focal mechanisms of the two different source models are shown as beach balls on top.

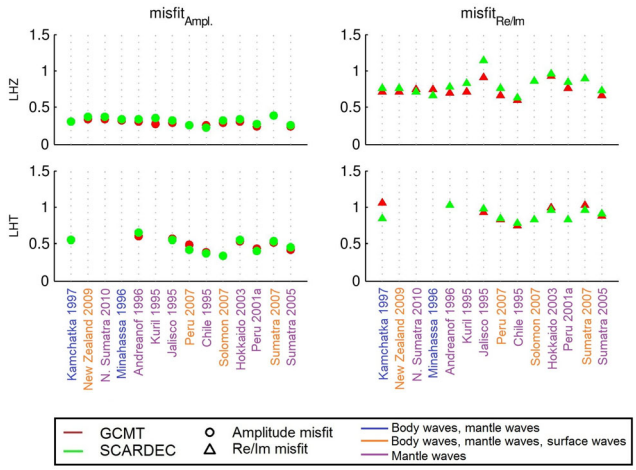

Figure 5. Amplitude (left-hand side) and Re/Im (right-hand side) misfit plots between data and GCMT synthetics (red), and data and SCARDEC synthetics (green) for the earthquakes ($M_w \geq 7.8$) where GCMT dip angles lay outside of SCARDEC dip angle intervals. In cases where not enough data were available (fewer than ten stations) no misfits were calculated (i.e. for the transverse component of the Kuril 1995, Minahassa 1996, New Zealand 2009 and N. Sumatra 2010 earthquakes). The SCARDEC amplitude and Re/Im misfits are on average 6–9 per cent larger than GCMT for vertical (LHZ) component data. For transverse (LHT) component data, SCARDEC and GCMT misfits are very similar. Earthquakes are plotted in ascending M_w order and their names are written in different colours according to the data used in the GCMT catalogue (blue for body and mantle waves, orange for body, mantle and surface waves, purple for mantle waves).

it is encouraging that SCARDEC source parameters explain long-period ($T \sim 3334$–250 s) 48-hr data spectra relatively well, despite being based only on the first 32 min of body-wave data after the earthquake, in comparison with GCMT, which uses much longer data time windows, and different long-period data types.

Fig. 5 shows larger differences between SCARDEC and GCMT misfits for spheroidal modes (vertical component) than for toroidal modes (transverse component). Specifically, the SCARDEC misfits for both the amplitude and the real and imaginary part of the FFT, are on average about 6–9 per cent larger than GCMT for vertical component data (mean misfit values are presented in Table 2). For toroidal modes, on average SCARDEC and GCMT source parameters explain the normal mode data equally well. This is probably related to the distinct characteristics of toroidal and spheroidal modes along with data noise issues. Love waves (and thus toroidal modes) are generally not as well excited by thrust earthquakes as Rayleigh waves. This, together with the fact that horizontal components are

Table 2. Mean misfit values (amplitude misfits and real and imaginary FFT misfits, see eqs 1–2) obtained over all the earthquakes studied in Section 3 from normal mode comparisons between GCMT and SCARDEC synthetics and real data, for both vertical and transverse components.

	Vertical component	Transverse component
$m^2_{\mathrm{ampl-GCMT}}$	0.30	0.48
$m^2_{\mathrm{ampl-SCARDEC}}$	0.32	0.48
$m^2_{\mathrm{Re/Im-GCMT}}$	0.76	0.92
$m^2_{\mathrm{Re/Im-SCARDEC}}$	0.81	0.90

Downloaded from https://academic.oup.com/gji/article/195/3/1989/627339 by guest on 14 October 2021

usually noisier than vertical components, may make it more difficult to distinguish slight differences in thrust earthquake source parameters when analysing love waves/toroidal modes.

4 BODY-WAVE 3-D FORWARD MODELLING TESTS

Shallow earthquake source inversions using broad-band body waves in the 0.003–0.03 Hz frequency range for earthquakes deeper than 5–10 km are relatively insensitive to the moment-dip trade-off (see, e.g. Figs S1–S4), so the SCARDEC method is expected to be able to resolve the two parameters independently. In order to test the quality of SCARDEC subduction earthquake dip angles and assess the impact of using simplified theories and Earth structure in the modelling (notably, ray theory on the 1-D IASP91 earth model, Kennett & Engdahl 1991), we use a more sophisticated seismic wave propagation tool to calculate body-wave data misfits. We use the SEM (Komatitsch & Tromp 1999) for the 3-D Earth crust CRUST2.0 (Bassin *et al.* 2000) and S20RTS (Ritsema *et al.* 1999) mantle models to calculate synthetic seismograms with high accuracy down to wave periods of $T \sim 17$ s. Although computationally expensive, the SEM is very accurate, in contrast with ray theory, which works under the assumption that the wavelength of the seismic waves is much smaller than the scale length of heterogeneity.

In order to examine the impact of the differences between SCARDEC and GCMT dip angles on the data fit, we consider all the 22 earthquakes selected in Section 2 for which GCMT dip angles lay outside of SCARDEC dip angle intervals. We calculate SEM theoretical seismograms for: (i) the SCARDEC source parameters and, (ii) all source parameters as in SCARDEC, except for the fault dip angle, which is taken from the GCMT catalogue. We bandpass filter synthetic displacement seismograms between 20 and 250 s and rotate the horizontal components into longitudinal and transverse components. Since the dominant period in the seismograms is shorter than the rupture time of the earthquakes studied, we convolve the synthetic seismograms with the average SCARDEC source time functions, smoothed at 1 s. We then filter and rotate the corresponding real displacement data in the same way as with the synthetics and calculate L_2-norm waveform data misfits for the two sets of synthetics:

$$m_{\mathrm{X}}^2 = \frac{\sum_i (d_i - s_i)^2}{\sum_i d_i^2}, \tag{3}$$

where d_i is the time-domain body-waveform at the ith station and s_i is the corresponding synthetic seismogram. X denotes the station component (Z for the vertical and T for the transverse component, respectively).

Fig. 6 shows examples of body-wave comparisons for the M_{w} 8.4 Peru 2001 earthquake, which occurred in the southern part of the Peru subduction zone. The main shock generated a relatively destructive tsunami and was followed by several large aftershocks. The rupture was unilateral and propagated to the SE for 320–400 km (Bilek & Ruff 2002; Giovanni *et al.* 2002; Melbourne & Webb 2002; Robinson *et al.* 2006). Only a few illustrative stations are shown in Fig. 6, but a larger number of stations for both the vertical (16) and the transverse components (15) are used to calculate waveform data misfits for the two sets of synthetics. The use of the GCMT dip angle yields a relatively poorer fit to the data ($m_{\mathrm{Z}}^2 = 0.30$ and $m_{\mathrm{T}}^2 = 0.23$ for vertical and transverse components, respectively) than SCARDEC ($m_{\mathrm{Z}}^2 = 0.22$ and $m_{\mathrm{T}}^2 = 0.16$), mainly in the amplitude and in a few cases in the phase of the signal. The largest differences are observed at SBA station on the vertical component and TAM station on the transverse component, where the SCARDEC dip angle leads to an improved body-wave data fit.

Fig. 7 shows the overall body-wave waveform misfit values calculated after modelling all the 22 earthquakes used in our study. The SCARDEC dip angles lead to similar or slightly better data fits in almost all cases for the vertical component, and for some earthquakes for the transverse component data. Despite being small, one needs to bear in mind that these variations in body-wave misfit are obtained by changing just one single earthquake source parameter—the dip

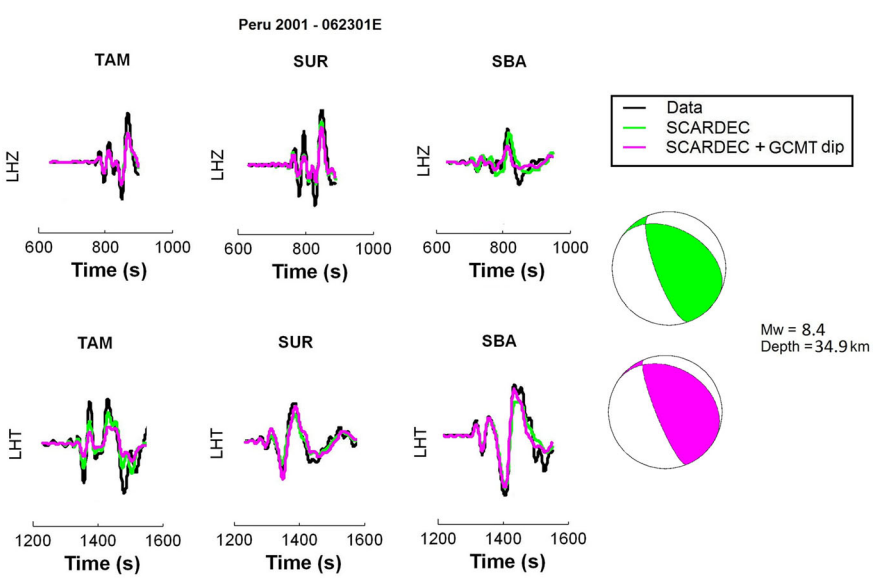

Figure 6. Illustrative examples of body-wave displacement comparisons for the M_{w} 8.4 Peru 2001 (GCMT code: 062301E) earthquake in vertical (top, *P* waves) and transverse (bottom, *SH* waves) components. Data are shown in black, SCARDEC synthetics in green and SCARDEC synthetics with the GCMT dip angle, in magenta. SCARDEC waveform misfits for vertical and transverse components over the total number of stations used (16 for the vertical and 15 for the transverse component) are: $m_{\mathrm{Z}}^2 = 0.22$ and $m_{\mathrm{T}}^2 = 0.16$ for SCARDEC dip angle, and $m_{\mathrm{Z}}^2 = 0.30$ and $m_{\mathrm{T}}^2 = 0.23$ for GCMT dip angle, respectively. Focal mechanisms of the two different source models are shown as beach balls on the right-hand side.

Downloaded from https://academic.oup.com/gji/article/195/3/1989/627339 by guest on 14 October 2021

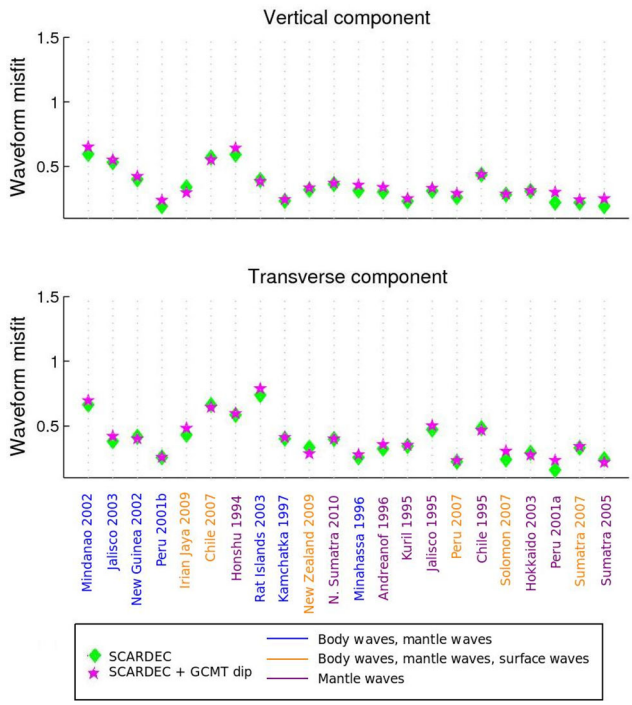

Figure 7. Waveform misfits between body-wave data and SCARDEC synthetics (green diamonds), and between data and SCARDEC synthetics with the GCMT dip (magenta stars) for all the earthquakes studied. The use of GCMT dip angles yields mean misfit values about 5 per cent larger than SCARDEC for vertical and transverse component data. Earthquakes are plotted in ascending M_w order and their names are written in different colours according to the data used in the GCMT inversions (blue for body and mantle waves, orange for body, mantle and surface waves, purple for mantle waves).

Table 3. Mean waveform misfit values obtained over all the earthquakes studied in Section 4 from body-wave comparisons between real data and 3-D SEM synthetics using either SCARDEC or GCMT ($m^2_{\mathrm{SCARDEC}(\delta_{\mathrm{GCMT}})}$) dip angles for both vertical and transverse components (see main text for details).

	Vertical component	Transverse component
m^2_{SCARDEC}	0.35	0.39
$m^2_{\mathrm{SCARDEC}(\delta_{\mathrm{GCMT}})}$	0.37	0.41

angle, not accounting for other types of trade-offs (e.g. moment-depth). Overall, the use of GCMT dip angles leads to an increase in the average body-wave misfit of about 5 per cent for both vertical and transverse components, showing that both GCMT and SCARDEC dip angles explain the data relatively well, with the SCARDEC dip angles leading to an apparent slightly improved data fit (see Table 3 for average misfit values over all the earthquakes). Nevertheless, it is worth pointing out that these dip angle comparisons are potentially affected by complications arising from the finite character of the rupture (subduction earthquakes typically rupture an interface with variable dip angle, along fault's strike and depth) and by the fact that whereas the GCMT method is based on estimations of the centroid in space and time, the SCARDEC method estimates source parameters for the PDE location. In addition, our misfit comparisons may also be influenced by possible trade-offs between the source parameters and the 3-D earth models used in the calculation of the synthetic seismograms. Hence, the significance of the apparent improvements in body-wave misfits using SCARDEC dip angles is not entirely clear.

5 COMPARISONS WITH OTHER STUDIES AND WITH GEOPHYSICAL CONSTRAINTS

Our independent tests of SCARDEC source parameters are further supported by comparisons with fault dip angles reported in individual earthquake studies published in the literature, using a wide range of data sets, like body waves (Sato *et al.* 1996; Zobin 1997; Kisslinger & Kikuchi 1997; Escobedo *et al.* 1998; Mendoza & Hartzell 1999; Gómez *et al.* 2000; Bilek & Ruff 2002; Giovanni *et al.* 2002; Yamanaka & Kikuchi 2003; Ito *et al.* 2004; Yagi 2004; Tavera *et al.* 2006; Ji 2007; Delouis *et al.* 2009; Furlong *et al.* 2009; Peyrat *et al.* 2010), surface waves (Tanioka *et al.* 1996; Robinson *et al.* 2006; Hébert *et al.* 2009), W-phase data (Kanamori & Rivera 2008), strong motion data (Koketsu *et al.* 2003; Honda *et al.* 2004), tsunami data (Ortiz *et al.* 1998; Lorito *et al.* 2008), geological and geodetic data, such as InSAR and GPS (Jordan *et al.* 1983; Melbourne *et al.* 1997; Miura *et al.* 2004; Miyazaki *et al.* 2004; Tanioka *et al.* 2007; Konca *et al.* 2008; Biggs *et al.* 2009; Chen *et al.* 2009; Béjar-Pizarro *et al.* 2010), summarized in Fig. 8. Moreover, we include comparisons with recent results from W-phase inversions (Duputel *et al.* 2012b) and from the Slab1.0 3-D subduction zone model (Hayes *et al.* 2012). To our knowledge, the Slab1.0 model is the most complete subduction zone compilation built so far by combining active source seismic data from geophysical surveys with information from the global Engdahl-Hilst-Buland (EHB) catalogue (Engdahl *et al.* 1998), NEIC PDE and GCMT earthquake catalogues, and with bathymetry data and sediment thickness maps. While ideally dip values averaged over the rupture area should be used, we use local Slab1.0 dip angle values at the GCMT source location, as the rupture areas are generally not known accurately for all the earthquakes considered. Nevertheless, we verified that Slab1.0 dip angles do not vary substantially within a circle with a 0.5° radius around the locations of the earthquakes (we found an average dip angle variability of 5°).

Fig. 8 shows that there is large scatter in published earthquake fault dip angle values, often spreading over a range of 20° or more (e.g. for New Guinea 2002, Rat Islands 2003, Peru 2007), with the Peru 2007 earthquake showing the largest variability (28°). The mean intraevent dip angle variability over all the earthquakes studied is 14°. In some cases the GCMT dip angles are the lowest end-members and the SCARDEC dip angles are the highest end-members, especially for earthquakes where there are not many dip angle values available from other studies (e.g. for Mindanao 2002, Irian Jaya 2009, New Zealand 2009).

GCMT dip angles determined using only long-period mantle waves (see earthquakes in purple font in Fig. 8) are always shallower than SCARDEC, and in most cases shallower than Slab1.0 or W-phase dip angles (e.g. Sumatra 2005, Hokkaido 2003, Jalisco 1995, Kuril 1995, N. Sumatra 2010, Honshu 1994). When body waves are also included in the GCMT inversions (earthquakes in blue and orange font in Fig. 8), for a few earthquakes GCMT dip angles are steeper than SCARDEC (Kamchatka 1997, Peru 2007, Solomon 2007).

Comparing SCARDEC and GCMT fault dip angles with those determined using the W-phase method and in the Slab1.0 model, we find that on average W-phase values are slightly closer to GCMT (with an average of absolute differences in dip angles between W-phase and GCMT of $\overline{|\delta^{\mathrm{GCMT}} - \delta^{\mathrm{W-phase}}|} = 4.7°$) than to SCARDEC ($\overline{|\delta^{\mathrm{SCARDEC}} - \delta^{\mathrm{W-phase}}|} = 5.3°$). In contrast, Slab1.0 fault dip angles show an overall better agreement with SCARDEC ($\overline{|\delta^{\mathrm{SCARDEC}} - \delta^{\mathrm{Slab1.0}}|} = 5.1°$) than with GCMT

Downloaded from https://academic.oup.com/gji/article/195/3/1989/627339 by guest on 14 October 2021

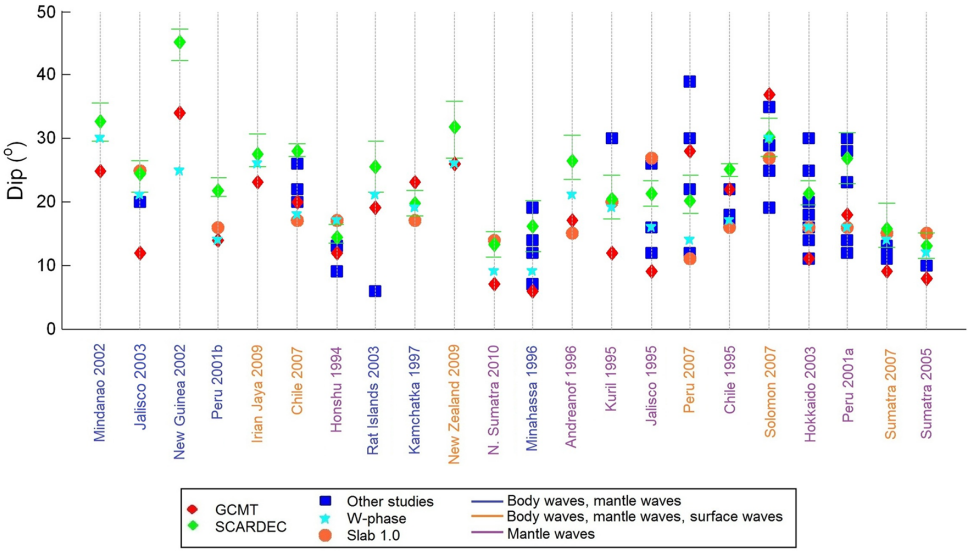

Figure 8. Dip angle comparisons between GCMT (red diamonds) and SCARDEC (green diamonds, including uncertainties) for earthquakes where GCMT dip angles lay outside of the SCARDEC dip angle intervals. Dip angles obtained from individual earthquake studies published in the literature (blue squares), W-phase inversions (cyan stars) and the Slab1.0 subduction zone model (Hayes *et al.* 2012, orange circles) are also shown, where available. Slab1.0 dip angles correspond to the GCMT locations (latitude and longitude). Slab1.0 depths may differ compared to GCMT depths, with Peru 2007 earthquake having the largest difference (20.8 km). The mean absolute difference is 6.6 km and the median is 5.0 km. Earthquakes are plotted in ascending M_w order and their names are written in different colour according to the data used by GCMT (blue for body and mantle waves, orange for body, mantle and surface waves, purple for mantle waves).

($|\overline{\delta^{\mathrm{GCMT}} - \delta^{\mathrm{Slab1.0}}}| = 7.3^\circ$). Nevertheless, these differences are relatively small and possibly not significant, thus rather highlighting that overall there is a reasonable agreement between SCARDEC and both Wphase and Slab1.0 dip angles, and better than with GCMT ($|\overline{\delta^{\mathrm{GCMT}} - \delta^{\mathrm{SCARDEC}}}| = 7.8^\circ$ for the 22 earthquakes considered in this section).

6 DISCUSSION

Despite tremendous advances in earthquake source imaging in the past decades, results produced by different agencies and/or research groups for the same earthquake often disagree (e.g. Weston *et al.* 2011, 2012), suggesting large uncertainties in the models. The problem is further compounded by the fact that earthquake model uncertainties are, if at all, only rarely quantified, and by the general lack of ground truth solutions. Thus, new source imaging benchmarking exercices and validation strategies are much needed for meaningful applications of earthquake source models (e.g. Mai *et al.* 2007, 2010; Hjörleifsdóttir & Ekström 2010). In order to objectively assess the quality of seismic source models and thus advance uncertainty quantification, it is important to go beyond classical resolution and/or misfit analyses. In particular, it is desirable to apply sophisticated modelling techniques to assess uncertainties due to simplified theoretical formulations and/or Earth structure employed to build the source models. Moreover, it is important to verify how well the models explain data not used in their construction for a full quantitative assessment of the robustness of the earthquake source models. This study addresses these issues and is thus well aligned with ongoing source validation efforts by carrying out new independent tests of large subduction zone earthquake source parameters estimated using SCARDEC, which is a recent fully automated body-wave technique for the fast determination of the seismic moment, focal mechanism, depth and source time functions. Despite only using the first 32 min of body-wave data after an earthquake, we find that SCARDEC source parameters (strike, rake, M_w and depth) for the subduction earthquakes studied agree generally well with those determined using longer data time windows, signals sensitive to lower frequencies and different inversion approaches (e.g. GCMT). Indeed, the GCMT and SCARDEC methods solve different mathematical problems (e.g. while the GCMT method determines moment tensor components, the SCARDEC technique solves directly for seismic moment, fault strike, dip and rake), with a different number of free parameters. Hence, the general agreement between SCARDEC and GCMT source parameters is encouraging, with the only clear systematic discrepancy occurring for fault dip angle estimates, where SCARDEC dip angles tend to be larger than GCMT. Our tests of these discrepancies show that SCARDEC source parameters explain independent 48-hr long, ultra-low-frequency normal mode data relatively well. Vallée *et al.* (2011) found similar results when testing how well SCARDEC source parameters explain shorter time-series (25 min) of long-period surface waves (150–200 s) for a smaller illustrative set of subduction earthquakes (17). By using longer time-series (48 hr), lower frequency normal mode data (0.1–4.0 mHz) and for a larger number of earthquakes (34), this study goes beyond the work of Vallée *et al.* (2011), providing a clearer and more general demonstration of the reliability of SCARDEC source parameters at explaining completely independent data sets. Indeed, several studies have shown that free oscillation data provide useful, independent information about earthquake sources (e.g. Park *et al.* 2005; Lambotte *et al.* 2006, 2007) compared to classic body and surface wave studies (e.g. Ishii *et al.* 2005; Tsai *et al.* 2005); however, the full potential of normal mode data for earthquake studies has not been studied yet, an issue that deserves to be further investigated in future work.

When using complete 3-D Earth synthetic seismograms computed using the highly accurate SEM, we find that SCARDEC fault

Downloaded from https://academic.oup.com/gji/article/195/3/1989/627339 by guest on 14 October 2021

dip angles explain real body-wave data as well or slightly better than GCMT dip angles, for the 3-D earth model considered. The slight deterioration in data fit when using GCMT dip angles might be due to the surface wave moment-dip trade-off affecting the GCMT source inversions for the earthquakes studied. Nevertheless, one needs to bear in mind that these dip angle comparisons are potentially affected by a number of complications, notably the fact that large subduction earthquakes tend to rupture an interface with a variable dip angle and possibly by trade-offs between source and Earth structure.

At first glance it may seem surprising that the trend of steeper SCARDEC dip angles than GCMT is not associated with an overall tendency for lower SCARDEC moment magnitudes than GCMT (see Fig. 2), for consistency with the GCMT moment-dip trade-off, as was reported by Vallée *et al.* (2011) for about half of the earthquakes in their study. As explained in Section 1, the updated SCARDEC magnitudes are slightly larger than those reported by Vallée *et al.* (2011), as a result of the improved high-pass filtering introduced in the automated version of the technique. In addition, there are a number of compounding factors, such as discrepancies in earthquake depth and SD. Indeed, for earthquakes with both similar SCARDEC and GCMT depth and SD, we do find that steeper SCARDEC dip angles are associated with lower moment magnitudes than GCMT, reflecting the GCMT surface wave dip-moment trade-off for shallow events (e.g. for the 2003 Hokkaido, or the 2005 and 2007 Sumatra earthquakes). However, for estimates based on methods like the GCMT technique, long-duration or shallow earthquakes require a larger moment magnitude to generate long-period seismic waves of the same amplitude than impulsive, shorter duration and deeper earthquakes. As some earthquakes are found shallower or longer duration by SCARDEC than GCMT (Fig. 2), this partly explains why SCARDEC magnitudes are not systematically smaller than GCMT. Moreover, the presence of long-duration tsunami earthquakes or complex events, which will be discussed later in the article, also tends to increase the SCARDEC magnitudes.

Comparisons of SCARDEC dip angles with those reported in other earthquake catalogues (GCMT and W-phase), in the Slab1.0 model and from individual earthquake studies in the literature show a large scatter in values reported for a given earthquake. This intraevent dip angle variability ranges from 6° to 28°, underlining the difficulties in constraining earthquake fault dip angles. The observed spread in dip estimates is consistent with previous findings. For example, Weston *et al.* (2011) report differences between 73 GCMT and InSAR-determined dip angles with a standard deviation of about 15°. Moreover, Ferreira *et al.* (2011) found an average intraevent variability of about 32° in fault dip estimates associated with the use of different earth models and theories in long-period CMT surface wave inversions. In addition, Hjörleifsdóttir & Ekström (2010) quantified the resolution and errors in GCMT source determinations due to unmodelled 3-D Earth structure and data noise using SEM synthetic data. They found that the fault dip angle can be underestimated by about 5° and that the seismic moment is overestimated by about 20 per cent for shallow subduction zone earthquakes when body-wave, surface wave and mantle wave data are used in the inversions. For earthquakes with $M_w \geq 7.5$, as in this paper, additional errors are expected because of the point source approximation used by GCMT. Our work, as well as these previous studies, highlight the need for quantitative uncertainty estimates to be reported along with the source parameters, particularly for subduction earthquake fault dip angles, which can strongly control tsunami run-up heights. Nevertheless, SCARDEC dip angle estimates are found to be broadly consistent with other reported values in the literature and slightly closer to those in the Slab1.0 model than GCMT.

Overall, the independent assessment of the SCARDEC method carried out in this study revealed its reliability in source parameter determinations of large subduction earthquakes. The fast and fully automated version currently operating routinely has a strong potential for tsunami alert purposes, with the plus of providing realistic source time functions compared to other fast methods such as the W-phase (Kanamori & Rivera 2008; Duputel *et al.* 2012b). This allows the rapid identification of long-duration tsunami earthquakes (Kanamori 1972), which have a source process anomalously long and smooth compared to that expected for their magnitude (e.g. Nicaragua 1992, N. Peru 1996, Java 2006, S. Sumatra 2010). In contrast, for example since 2004 the GCMT method assumes a triangular source time function (and before that a boxcar function) with half-duration determined by a constant stress drop scaling relation to the seismic moment.

Fig. 9 compares the average SCARDEC source time functions (green) with rupture duration estimates from various individual earthquake studies. Blue vertical lines in Fig. 9 correspond to SD estimates obtained mainly by body-waves, and in a few cases by body and surface waves (Johnson *et al.* 1995; Sato *et al.* 1996; Tanioka *et al.* 1996; Delouis *et al.* 1997; Ihmlé & Ruegg 1997; Kisslinger & Kikuchi 1997; Tanioka & Ruff 1997; Zobin 1997; Ihmlé *et al.* 1998; Carlo *et al.* 1999; Mendoza & Hartzell 1999; Swenson & Beck 1999; Gómez *et al.* 2000; Abercrombie *et al.* 2001; Zobin & Levina 2001; Bilek & Ruff 2002; Giovanni *et al.* 2002; Henry & Das 2002; Yamanaka & Kikuchi 2003; Yagi 2004; Ammon *et al.* 2006; Robinson *et al.* 2006; Tavera *et al.* 2006; Bilek & Engdahl 2007; Bukchin & Mostinskii 2007; Ammon *et al.* 2008; Konca *et al.* 2008; Nakano *et al.* 2008; Biggs *et al.* 2009; Lay *et al.* 2010a,b, 2011; Peyrat *et al.* 2010; Poiata *et al.* 2010; Lee *et al.* 2011; Honda *et al.* 2011; Zhang *et al.* 2012). For reference, we also show triangular/boxcar source time functions with SD calculated using the same scaling relation as used by the GCMT (red), and $2\tau_c$ values (brown vertical lines), where τ_c is the GCMT centroid time-delay, which can be considered a good approximation of the SD (Duputel *et al.* 2013) for the 34 subduction earthquakes considered in Section 2. Indeed, comparisons of $2\tau_c$ values with SCARDEC SDs show an average absolute difference of approximately 15 s. Interplate thrust earthquakes shallower than 50 km such as those studied here are usually characterized by lower stress drops and longer SDs than other kinds of earthquakes such as, normal and/or thrust intraplate earthquakes (Allmann & Shearer 2009). The shape and duration of their source time functions are likely related to the rheology of different subduction zones, among other factors (Houston 2001). Fig. 9 shows that overall there is a good agreement between the rupture durations obtained using SCARDEC and the majority of the values reported in individual studies. The only exception is for the M_w 7.5 Molucca Sea event, where the study by Nakano *et al.* (2008) reports a rupture duration of 16 s for this event based on a new frequency-domain waveform technique. Nevertheless, the authors do acknowledge that the value that they obtain is shorter than that expected for a M_w 7.5 event (26 s for the constant stress drop scaling relation used by the GCMT, which agrees well with the SCARDEC estimate). Although for some $M_w \leq 7.8$ events there is indeed a good agreement between SCARDEC and the triangular/boxcar source time functions used by the GCMT (e.g. for the Peru 2001b, New Guinea 2002, Irian Jaya 2009 and New Zealand 2009 earthquakes), SCARDEC generally leads to longer SDs (except for Minahassa 1996 and Jalisco 2003). Importantly,

Downloaded from https://academic.oup.com/gji/article/195/3/1989/627339 by guest on 14 October 2021

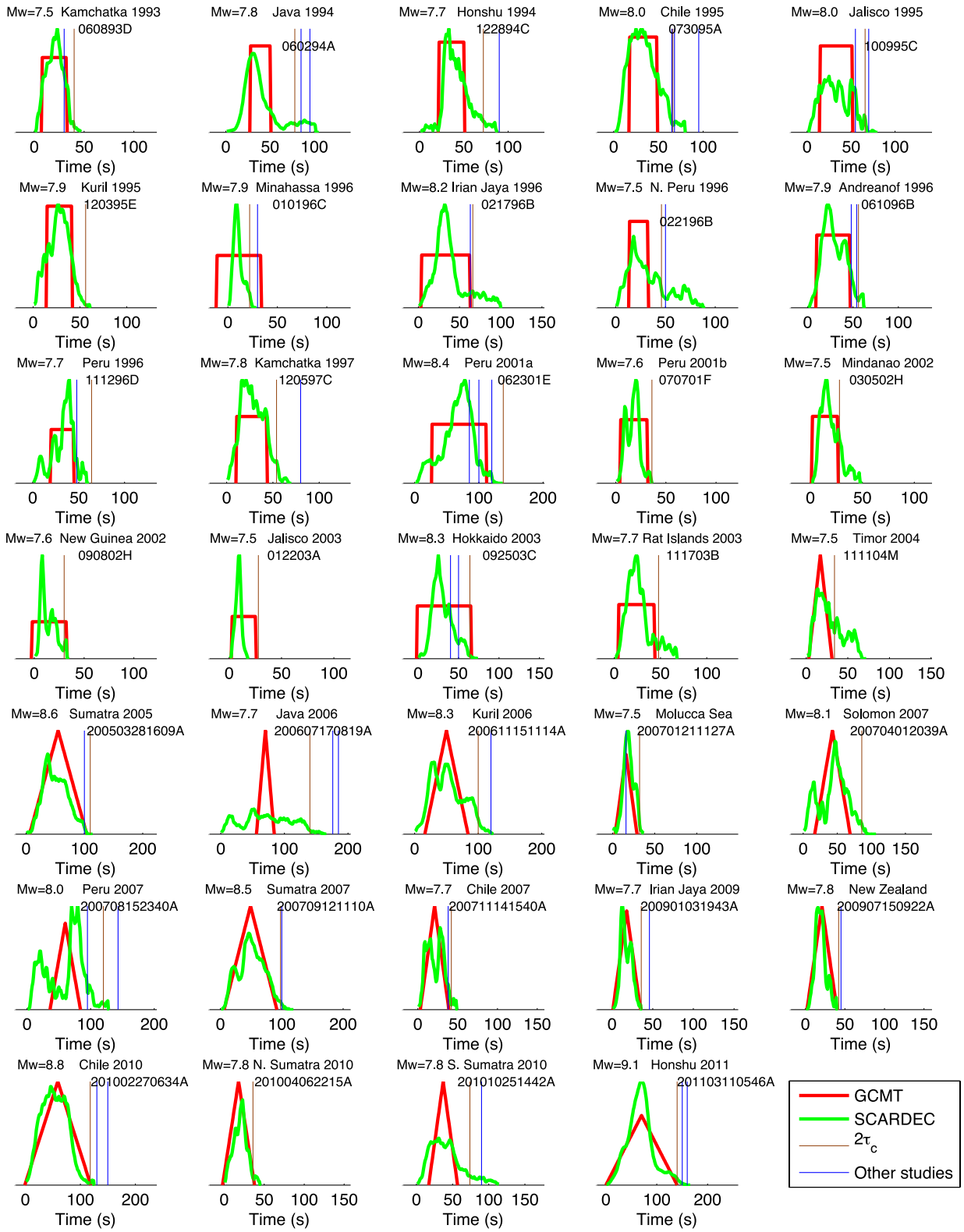

Figure 9. Comparison between SCARDEC average source time functions (green) with rupture durations estimated from individual earthquake studies (blue vertical lines; see main text and Table S2) and $2\tau_c$ values (brown vertical lines; see main text). For reference, we also show triangular/boxcar source time functions with rupture duration estimated from a constant stress drop scaling relation, as used by the GCMT catalogue (red), for the 34 subduction earthquakes considered in this paper. GCMT source time functions are represented as boxcar functions for earthquakes that occurred before 2004. After the 1st of January 2004 the GCMT source time function is assumed to be triangular (Ekström *et al.* 2012). Zero time corresponds to the PDE time of each earthquake. Earthquake names, GCMT magnitudes and codes are shown on top of each plot. Three cases of long-duration tsunami earthquakes are identified (M_w 7.5 N. Peru 1996–022196B, M_w 7.7 Java 2006–200607170819A, M_w 7.8 S. Sumatra 2010–201010251442A) by SCARDEC, having smoother and longer source time functions than expected from their moment magnitude.

Downloaded from https://academic.oup.com/gji/article/195/3/1989/627339 by guest on 14 October 2021

SCARDEC source time functions allow the clear identification of long-duration tsunami earthquakes (e.g. N. Peru 1996, Java 2006, S. Sumatra 2010), as well as of complex events (Peru 2007). The M_w 7.5 N. Peru 1996 event (022196B) is a long-duration tsunami earthquake (Polet & Kanamori 2000), having generated a larger tsunami than expected from its surface wave magnitude, $M_s = 6.6$ (Heinrich *et al.* 1998). Moreover, its body-wave magnitude is significantly lower ($m_b = 5.8$) than the moment magnitude, and the associated tsunami was characterized by run-up heights of 1–5 m along a coastline of 400 km (Bourgeois *et al.* 1999). There is a discrepancy between SCARDEC SD (∼80 s) and those by Ihmlé *et al.* (1998) and $2\tau_c$ (∼50 s). However, the late part of the SCARDEC source time function (50–80 s) corresponds to only 20 per cent of the total moment, possibly resolved because the SCARDEC technique does not impose a simple source time function shape, but it rather deconvolves it from actual seismic data. Similarly, the M_w 7.7 Java 2006 earthquake (200607170819A) caused a deadly tsunami with run-up heights up to 8 m to the south coast of Java. The main shock is a long-duration tsunami earthquake with a significant discrepancy between its surface magnitude ($M_s = 7.7$) and body-wave magnitude ($m_b = 6.1$), characterized by an unusually low rupture velocity (1.0–1.5 km s^{-1}). The rupture included five to six episodes of moment release on a smooth and long source time function of 185 s (Ammon *et al.* 2006). Finally, the M_w 7.8 S. Sumatra 2010 earthquake (201010251442A) caused a tsunami with run-up heights up to 9 m along the southwestern coasts of Pagai islands, significantly higher than expected, given its magnitude. The rupture time which was found by independent studies (Lay *et al.* 2011; Newman *et al.* 2011), 90–125 s, much longer than the duration used by the GCMT, is in good agreement with SCARDEC. Moreover, the main shock was characterized as a slow event with a rupture velocity of 1.5 km s^{-1} and with a long-duration tsunami earthquake difference between surface magnitude ($M_s = 7.8$) and body-wave magnitude ($m_b = 6.5$).

The SCARDEC source time functions also enable us to identify some complex features in the rupture history of the earthquakes in our data set, with the M_w 8.0 Peru 2007 earthquake (200708152340A) being one of the most prominent cases. The main shock caused strong damage to the city of Pisco and was followed by a significant local tsunami with run-up heights up to 10 m at the Paracas peninsula (Sladen *et al.* 2010). While the earthquake has a GCMT source half-duration of 23.5 s, its SCARDEC source time function highlights the complex character of this rupture with two different episodes and a total SD of 121 s. Indeed, other studies reported a slip history of the main shock being characterized by the presence of two distinct patches, rupturing a total fault area of about 300 km by 160 km. The first patch was located close to the hypocentre and the second, which was larger, ruptured to the south around 60 s later (Motagh *et al.* 2008; Sladen *et al.* 2010), in good agreement with SCARDEC's source time function.

All these examples clearly show the power of the SCARDEC method for the rapid discrimination of long-duration tsunami events and of complex rupture patterns, underlining its strong potential for seismic monitoring and tsunami warning efforts. In practice, SCARDEC's source time functions could be used in an automated way to identify tsunami subduction earthquakes using criteria such as: (i) earthquake depth being shallower than around 25 km; (ii) the source time function having a duration at least 1.5–2 times longer than the values determined by a scaling relation with respect to the obtained seismic moment (e.g. as in GCMT) and, (iii) the source time function peak moment rate being at least 1.5–2 times lower than that in a triangular source time function corresponding to the half-duration obtained by the scaling relation mentioned in criterion (ii).

7 CONCLUSIONS

We have tested the robustness and reliability of SCARDEC source parameters for major ($M_w \geq 7.5$) shallow subduction earthquakes of the past 20 yr. We found an overall good agreement between SCARDEC and GCMT source parameters except for the fault dip angle, for which the SCARDEC values were found on average steeper than GCMT solutions. We examined these discrepancies and validated the method by showing that overall SCARDEC source parameters explain independent long-period, 48-hr normal mode data spectra reasonably well, despite using only the first 32 min of body-wave data following the earthquake. Using accurate purely numerical forward modelling of body-wave data on a 3-D earth model, we found that the SCARDEC dip angles explain body-wave data as well or slightly better than the GCMT method. SCARDEC dip angles showed also a good agreement with values from other individual earthquake studies and with subduction slab geophysical constraints. In addition, unlike some other routine source inversion methods, SCARDEC estimates realistic source time functions, enabling the rapid identification of long-duration tsunami earthquakes with anomalously large SDs compared to their magnitudes and the modelling of the associated complex seismic waveforms. Thus, the SCARDEC method complements existing routine seismic monitoring techniques and offers a strong potential for applications in ocean-wide tsunami warning.

ACKNOWLEDGEMENTS

We thank Göran Ekström, Zacharie Duputel and three anonymous reviewers for their interesting comments which helped us to improve the manuscript. We gratefully acknowledge the availability of global seismograms from the FDSN global network and the IRIS Data Centre. This work has been supported by the European Commission's Initial Training Network project QUEST (contract FP7-PEOPLE-ITN-2008-238007, www.quest-itn.org). The research presented in this paper was carried out on the high performance computing cluster supported by the Research and Specialist Computing Support service at the University of East Anglia and at the UK NERC-EPSRC National Supercomputing facilities HECToR. AMGF and MV thank support from the Alliance: Franco-British Partnership Programme 2010 (Project 10.007).

REFERENCES

Abercrombie, R., Antolik, M., Felzer, K. & Ekström, G., 2001. The 1994 Java tsunami earthquake: slip over a subducting seamount, *J. geophys. Res.,* **106**(B4), 6595–6607.

Allmann, B.P. & Shearer, P.M., 2009. Global variations of stress drop for moderate to large earthquakes, *J. geophys. Res.,* **114,** B01310, doi:10.1029/2008JB005821.

Ammon, C.J., Kanamori, H., Lay, T. & Velasco, A.A., 2006. The 17 July 2006 Java tsunami earthquake, *Geophys. Res. Lett.,* **33,** L24308, doi:10.1029/2006GL028005.

Ammon, C.J., Kanamori, H. & Lay, T., 2008. A great earthquake doublet and seismic stress transfer cycle in the central Kuril islands, *Nature,* **451**(7178), 561–565.

Bassin, C., Laske, G. & Masters, G., 2000. The current limits of resolution for surface wave tomography in North America, *EOS, Trans. Am. geophys. Un.,* **81,** F897 Fall Meet. Suppl., Abstract S12A-03.

Béjar-Pizarro, M. *et al.*, 2010. Asperities and barriers on the seismogenic zone in North Chile: state-of-the-art after the 2007 Mw 7.7 Tocopilla

Downloaded from https://academic.oup.com/gji/article/195/3/1989/627339 by guest on 14 October 2021

earthquake inferred by GPS and InSAR data, *Geophys. J. Int.,* **183,** 390–406.

Biggs, J., Robinson, D.P. & Dixon, T.H., 2009. The 2007 Pisco, Peru, earthquake (M8.0): seismology and geodesy, *Geophys. J. Int.,* **176,** 657–669.

Bilek, S. & Engdahl, E.R., 2007. Rupture characterization and aftershock relocations for the 1994 and 2006 tsunami earthquakes in the Java subduction zone, *Geophys. Res. Lett.,* **34,** L20311, doi:10.1029/2007GL031357.

Bilek, S.L. & Ruff, L.J., 2002. Analysis of the 23 June 2001 Mw = 8.4 Peru underthrusting earthquake and its aftershocks, *Geophys. Res. Lett.,* **29**(20), 1960, doi:10.1029/2002GL015543.

Borrero, J.C., Weiss, R., Okal, E.A., Hidayat, R., Suranto Arcas, D. & Titov, V.V., 2009. The tsunami of 2007 September 12, Bengkulu province, Sumatra, Indonesia: post-tsunami field survey and numerical modelling, *Geophys. J. Int.,* **178,** 180–194.

Bouchon, M., 1976. Teleseismic body wave radiation from a seismic source in a layered medium, *Geophys. J. R. astr. Soc.,* **47,** 515–530.

Bourgeois, J. *et al.*, 1999. Geologic setting, field survey and modeling of the Chimbote, northern Peru tsunami of 21 February 1996, *Pure appl. Geophys.,* **154,** 513–540.

Bukchin, B.G. & Mostinskii, A.Z., 2007. Integral source characteristics of the Sumatra earthquakes of December 26, 2004, and March 28, 2005, *J. Volcan. Seism.,* **1**(4), 263–273.

Carlo, D., Lay, T., Ammon, C.J. & Zhang, J., 1999. Rupture process of the 1995 Antofagasta subduction earthquake (Mw = 8.1), *Pure appl. Geophys.,* **154,** 677–709.

Chen, T., Newman, A.V., Feng, L. & Fritz, H.M., 2009. Slip distribution from the 1 April 2007 Solomon Islands earthquake: a unique image of near-trench rupture, *Geophys. Res. Lett.,* **36,** L16307, doi:10.1029/2009GL039496.

Delouis, B. *et al.*, 1997. The Mw = 8.0 Antofagasta (North Chile) earthquake of 30 July 1995: a percursor to the end of the large 1877 gap, *Bull. seism. Soc. Am.,* **87**(2), 427–445.

Delouis, B., Pardo, M., Legrand, D. & Monfret, T., 2009. The Mw 7.7 Tocopilla earthquake of 14 November 2007 at the southern edge of the Northern Chile Seismic Gap: rupture in the deep part of the coupled plate interface, *Bull. seism. Soc. Am.,* **99**(1), 87–94.

Duputel, Z., Rivera, L., Fukahata, Y. & Kanamori, H., 2012a. Uncertainty estimations for seismic source inversions, *Geophys. J. Int.,* **190**(2), 1243–1256.

Duputel, Z., Rivera, L., Kanamori, H. & Hayes, G., 2012b. Wphase source inversion for moderate to large earthquakes (1990–2010), *Geophys. J. Int.,* **189**(2), 1125–1147.

Duputel, Z., Tsai, V.C., Rivera, L. & Kanamori, H., 2013. Using centroid time-delays to characterize source durations and identify earthquakes with unique characteristics, *Earth planet. Sci. Lett.,* **374,** 92–100.

Dziewonski, A.M. & Anderson, D.L., 1981. Preliminary reference Earth model, *Phys. Earth Planet. Int.,* **25,** 297–356.

Dziewonski, A.M., Chou, T.A. & Woodhouse, J.H., 1981. Determination of earthquake source parameters from waveform data for studies of global and regional seismicity, *J. geophys. Res.,* **86(B4),** 2825–2852.

Ekström, G., Nettles, M. & Dziewonski, A.M., 2012. The global CMT Project 2004–2010: centroid-moment tensors for 13,017 earthquakes, *Phys. Earth planet. Int.,* **200–201,** 1–9.

Engdahl, E.R., Van Der Hilst, R.D. & Buland, R.P., 1998. Global teleseismic earthquake relocation with improved travel times and procedures for depth determination, *Bull. seism. Soc. Am.,* **88,** 722–743.

Escobedo, D., Pachero, J.F. & Suárez, G., 1998. Teleseismic body-wave analysis of the 9 October, 1995 (Mw = 8.0), Colima-Jalisco, Mexico earthquake, and its largest foreshock and aftershock, *Geophys. Res. Lett.,* **25**(4), 547–550.

Ferreira, A.M.G., Weston, J. & Funning, G.J., 2011. Global compilation of interferometric synthetic aperture radar earthquake source models: 2. Effects of 3-D Earth structure. *J. geophys. Res.,* **116,** B08409, doi:10.1029/2010JB008132.

Furlong, K.P., Lay, T. & Ammon, C.J., 2009. A great earthquake rupture across a rapidly evolving three-plate boundary, *Science,* **324**(5924), 226–229.

Gilbert, F. & Dziewonski, A.M., 1975. An application of normal mode theory to the retrieval of structural parameters and source mechanisms from seismic spectra, *Phil. Trans. R. Soc. Lond.,* **278,** 187–269.

Giovanni, M.K., Beck, S.L. & Wagner, L., 2002. The June 23, 2001 Peru earthquake and the southern Peru subduction zone, *Geophys. Res. Lett.,* **29**(21), 2018, doi:10.1029/2002GL015774.

Gómez, J.M., Madariaga, R., Walpersdorf, A. & Chalard, E., 2000. The 1996 earthquakes in Sulawesi, Indonesia, *Bull. seism. Soc. Am.,* **90**(3), 739–751.

Hayes, G.P., Rivera, L. & Kanamori, H., 2009. Source inversion of the W-Phase: real-time implementation and extension to low magnitudes, *Seismol. Res. Lett.,* **80,** 817–822.

Hayes, G.P., Wald, D.J. & Johnson, R.L., 2012. Slab1.0: a three-dimensional model of global subduction zone geometries, *J. geophys. Res.,* **117,** B01302, doi:10.1029/2011JB008524.

Hébert, H., Reymond, D., Krien, Y., Vergoz, J., Scindelé, F., Roger, J. & Loevenbruck, A., 2009. The 15 August 2007 Peru earthquake and tsunami: influence of the source characterisitcs on the tsunami heights, *Pure appl. Geophys.,* **166,** 211–232.

Heinrich, P., Schindelé, F. & Guibourg, S., 1998. Modeling of the February 1996 Peruvian tsunami, *Geophys. Res. Lett.,* **25**(14), 2687–2690.

Henry, C. & Das, S., 2002. The Mw 8.2, 17 February 1996 Biak, Indonesia, earthquake: rupture history, aftershocks, and fault plane properties, *J. geophys. Res.,* **107**(B11), 2312, doi:10.1029/2001JB000796.

Hjörleifsdóttir, V. & Ekström, G., 2010. Effects of three-dimensional Earth structure on CMT earthquake parameters, *Phys. Earth planet. Int.,* **179,** 178–190.

Honda, R., Aoi, S., Morikawa, N., Sekiguchi, H., Kunugi, T. & Fujiwara, H., 2004. Ground motion and rupture process of the 2003 Tokachi-oki earthquake obtained from strong motion data of K-NET and KiK-net, *Earth Planets Space,* **56,** 317–322.

Honda, R. *et al.*, 2011. A complex rupture image of the 2011 Tohoku earthquake revealed by the MeSO-net, *Earth Planets Space,* **63,** 583–588.

Houston, H., 2001. Influence of depth, focal mechanism, and tectonic setting on the shape and duration of earthquake source time functions, *J. geophys. Res.,* **106**(B6), 11 137–11 150.

Ihmlé, P.F., Gomez, J.-M., Heinrich, P. & Guibourg, S., 1998. The 1996 Peru tsunami-genic earthquake: broadband source process, *Geophys. Res. Lett.,* **25**(14), 2691–2694.

Ihmlé, P. & Ruegg, J.C., 1997. Source tomography by simulated annealing using broad-band surface waves and geodetic data: application to the Mw = 8.1 Chile 1995 event, *Geophys. J. Int.,* **131,** 146–158.

Ishii, M., Shearer, P.M., Houston, H. & Vidale, J.E., 2005. Extent, duration and speed of the 2004 Suamtra-Andaman earthquake imaged by the Hi-net array, *Nature,* **435,** 933–936.

Ito, Y., Matsubayashi, H., Kimura, H., Matsumoto, T., Asano, Y. & Sekiguchi, S., 2004. Spatial distribution for moment tensor solutions of the 2003 Tokachi-oki earthquake (MJMA = 8.0) and aftershocks, *Earth Planets Space,* **56,** 301–306.

Ji, C., 2007. Preliminary result of the Sep 12, 2007 Sumatra earthquake, available at http://earthquake.usgs.gov/earthquakes/eqinthenews/2007/us2007aqbk/finite_fault.php.

Johnson, J.M., Tanioka, Y., Satake, K. & Ruff, L.J., 1995. Two 1993 Kamchatka Earthquakes, *Pageoph.,* **144,** 633–647.

Jordan, T.E., Isacks, B.L., Allmendinger, R.W., Brewer, J.A., Ramos, V.A. & Ando, C.J., 1983. Andean tectonics related to geometry of subducted Nazca plate, *Geol. St. Am. Bull.,* **94,** 341–361.

Kanamori, H., 1972. Mechanism of tsunami earthquakes, *Phys. Earth planet. Inter.,* **6,** 356–359.

Kanamori, H. & Given, J.W., 1981. Use of long-period surface waves for rapid determination of earthquake-source parameters, *Phys. Earth planet. Inter.,* **27,** 8–31.

Kanamori, H. & Rivera, L., 2008. Source inversion of W phase: speeding up seismic tsunami warning, *Geophys. J. Int.,* **175,** 222–238.

Kennett, B.L. N. & Engdahl, E.R., 1991. Travel times for global earthquake location and phase association, *Geophys. J. Int.,* **105,** 429–465.

Downloaded from https://academic.oup.com/gji/article/195/3/1989/627339 by guest on 14 October 2021

Kisslinger, C. & Kikuchi, M., 1997. Aftershocks of the Andreanof islands earthquake of June 10, 1996, and local seismotectonics, *Geophys. Res. Lett.,* **24**(15), 1883–1886.

Koketsu, K., Hikima, K., Miyazaki, S. & Ide, S., 2003. Joint inversion of strong motion and geodetic data for the source process of the 2003 Tokachi-oki, Hokkaido, earthquake, *Earth Planets Space,* **55,** 1–6.

Komatitsch, D. & Tromp, J., 1999. Introduction to the spectral element method for three-dimensional seismic wave propagation, *Geophys. J. Int.,* **139,** 806–822.

Konca, A.O. *et al.*, 2008. Partial rupture of a locked patch of the Sumatra megathrust during the 2007 earthquake sequence, *Nature,* **456,** 631–635.

Lambotte, S., Rivera, L. & Hinderer, J., 2006. Rupture length and duration of the 2004 Aceh-Sumatra earthquake from the phases of the Earth's gravest free oscillations, *Geophys. Res. Lett.,* **33,** L023307, doi:10.1029/2005GL024090.

Lambotte, S., Rivera, L. & Hinderer, J., 2007. Constraining the overall kinematics of the 2004 Sumatra and the 2005 Nias earthquakes using the Earth's gravest free oscillations, *Bull. seism. Soc. Am.,* **97**(1A), S128–S138.

Lay, T., Ammon, C.J., Hutko, A.R. & Kanamori, H., 2010a. Effects of kinematic constraints on teleseismic finite-source rupture inversions: Great Peruvian earthquakes of 23 June 2001 and 15 August 2007, *Bull. seism. Soc. Am.,* **100**(3), 969–994.

Lay, T., Ammon, C.J., Kanamori, H., Koper, K., Sufri, O. & Hutko, A.R., 2010b. Teleseismic inversion for rupture process of the 27 February 2010 Chile (Mw 8.8) earthquake, *Geophys. Res. Lett.,* **37,** L13301, doi:10.1029/2010GL043379.

Lay, T., Ammon, C.J., Kanamori, H., Yamazaki, Y., Cheung, K.F. & Hutko, A.A., 2011. The 25 October 2010 Mentawai tsunami earthquake (Mw 7.8) and the tsunami hazard presented by shallow megathrust ruptures, *Geophys. Res. Lett.,* **38,** L06302, doi:10.1029/2010GL046552.

Lee, S.-J., Huang, B.-S., Ando, M., Chiu, H.-C. & Wang, J.-H., 2011. Evidence of large scale repeating slip during the 2011 Tohoku-Oki earthquake, *Geophys. Res. Lett.,* **38,** L19306, doi:10.1029/2011GL049580.

Lorito, S., Romano, F., Piatanesi, A. & Boschi, E., 2008. Source process of the September 12, 2007. Mw 8.4 southern Sumatra earthquake from tsunami tide gauge record inversion, *Geophys. Res. Lett.,* **35,** L02310, doi:10.1029/2007GL032661.

Mai, P.M., Burjanek, J., Delouis, B., Festa, G., Francois-Holden, C., Monelli, D., Uchide, T. & Zahradnik, J., 2007. Earthquake source inversion blindtest: initial results and further developments, *EOS, Trans. Am. geophys. Un.,* **88,** 52.

Mai, P.M., Page, M.T. & Schorlemmer, D., 2010. Source inversion validation: quantifying uncertainties in earthquake source inversions, *EOS, Trans. Am. geophys. Un.,* **91,** 49.

Melbourne, T., Carmichael, I., DeMets, C., Hudnut, K., Sanchez, O., Stock, J., Suarez, G. & Webb, F., 1997. The geodetic signature of the M8.0 Oct. 9, 1995, Jalisco subduction earthquake, *Geophys. Res. Lett.,* **24**(6), 715–718.

Melbourne, T.I. & Webb, F.H., 2002. Precursory transient slip during the 2001 Mw = 8.4 Peru earthquake sequence from continious GPS, *Geophys. Res. Lett.,* **29**(21), 2032, doi:10.1029/2002GL015533.

Mendoza, C. & Hartzell, S., 1999. Fault-slip distribution of the 1995 Colima-Jalisco, Mexico, earthquake, *Bull. seism. Soc. Am.,* **89**(5), 1338–1344.

Miura, S., Hasegawa, A., Suwa, Y. & Nishimura, T., 2004. The 2003 M8.0 Tokachi-Oki earthquake—how much has the great event paid back slip debts?, *Geophys. Res. Lett.,* **31,** L05613, doi:10.1029/2003GL019021.

Miyazaki, S. *et al.*, 2004. Modeling the rupture process of the 2003 September 25 Tokachi-Oki (Hokkaido) earthquake using 1-Hz GPS data, *Geophys. Res. Lett.,* **31,** L06623, doi:10.1029/2003GL019410.

Motagh, M., Wang, R., Walter, T.R., Bürgmann, R., Fielding, E., Anderssohn, J. & Zschau, J., 2008. Coseismic slip model of the 2007 August Pisco earthquake (Peru) as constrained by Wide Swath radar observations, *Geophys, J. Int.,* **174,** 842–848.

Nabelek, J., 1984. Determination of earthquake fault parameters from inversion of body waves, *PhD thesis,* Mass. Inst. of Technol., 361 pp., Cambridge, MA.

Nakano, M., Kumagai, H. & Inoue, H., 2008. Waveform inversion in the frequency domain for the simultaneous determination of earthquake source mechanism and moment function, *Geophys. J. Int.,* **173,** 1000–1011.

Newman, A.V., Hayes, G., Wei, Y. & Convers, J., 2011. The 25 October 2010 Mentawai tsunami earthquake, from real-time discriminants, finite-fault rupture, and tsunami excitation, *Geophys. Res. Lett.,* **38,** L05302, doi:10.1029/2010GL046498.

Ortiz, M., Singh, S.K., Pachero, J. & Kostoglodov, V., 1998. Rupture length of the October 9, 1995 Colima-Jalisco earthquake (Mw 8.0) estimated from tsunami data, *Geophys. Res. Lett.,* **25**(15), 2857–2860.

Park., J. *et al.*, 2005. Earth's free oscillations excited by the 26 December 2004 Sumatra-Andaman earthquake, *Science,* **308,** 1139–1144.

Peyrat, S., Madariaga, R., Buforn, E., Campos, J., Asch, G. & Vilotte, J.P., 2010. Kinematic rupture process of the 2007 Tocopilla earthquake and its main aftershocks from teleseismic and strong-motion data, *Geophys, J. Int.,* **182,** 1411–1430.

Poiata, N., Koketsu, K. & Miyake, H., 2010. Source processes of the 2009 Irian Jaya, Indonesia, earthquake doublet, *Earth Planets Space,* **62,** 475–481.

Polet, J. & Kanamori, H., 2000. Shallow subduction zone earthquakes and their tsunamigenic potential, *Geophys, J. Int.,* **142,** 684–702.

Ritsema, J., Van Heijst, H.J. & Woodhouse, J.H., 1999. Complex shear velocity structure imaged beneath Africa and Iceland, *Science,* **286,** 243–259.

Robinson, D.P., Das, S. & Watts, A.B., 2006. Earthquake rupture stalled by a subducting fracture zone, *Science,* **312,** 1203–1205.

Sato, T., Imanishi, K. & Kasuga, M., 1996. Three-stage rupture process of the 28 December 1994 Sanriku-Oki earthquake, *Geophys. Res. Lett.,* **23**(1), 33–36.

Sladen, A. *et al.*, 2010. Source model of the 2007 Mw 8.0 Pisco, Peru earthquake: implications for seismogenic behavior of subduction megathrusts, *J. geophys. Res.,* **115,** B02405, doi:10.1029/2009JB006429.

Swenson, J.L. & Beck, S.L., 1999. Source characteristics of the 12 November 1996 Mw 7.7 Peru subduction zone earthquake, *Pure appl. Geophys.,* **154,** 731–751.

Tanioka, Y., Ruff, L. & Satake, K., 1996. The Sanriku-oki, Japan, earthquake of December 28, 1994 (Mw 7.7): rupture of a different asperity from a previous earthquake, *Geophys. Res. Lett.,* **23**(12), 1465–1468.

Tanioka, Y & Ruff, L.J., 1997. Source time functions, *Seism. Res. Lett.,* **68**(3), 386–400.

Tanioka, Y., Namegaya, Y., Nishimura, Y., Yoshinobu, T., Nakamura, Y., Murata, M. & Woodward, S., 2007. Fault model of the 2007 Solomon earthquake estimated from the crustal deformation survey data, *AGU Fall Meeting 2007,* Abstract S13A–1044.

Tavera, H. *et al.*, 2006. The southern region of Peru earthquake of June 23rd, 2001, *J. Seism.,* **10**(2), 171–195.

Tsai, V.C., Hayes, G.P. & Duputel, Z., 2011. Constraints on the long-period moment-dip tradeoff for the Tohoku earthquake, *Geophys. Res. Lett.,* **38,** L00G17, doi:10.1029/2011GL049129.

Tsai, V.C., Nettles, M., Ekström, G. & Dziewonski, A.M., 2005. Multiple CMT source analysis of the 2004 Sumatra earthquake, *Geophys. Res. Lett.,* **32,** L17304, doi 10.1029/2005GL023813.

Vallée, M., Charléty, J., Ferreira, A.M.G., Delouis, B. & Vergoz, J., 2011. SCARDEC: a new technique for the rapid determination of seismic moment magnitude, focal mechanism and source time functions for large earthquakes using body-wave deconvolution, *Geophys. J. Int.,* **184,** 338–358.

Weston, J., Ferreira, A.M.G. & Funning, G.J., 2011. Global compilation of interferometric synthetic aperture radar earthquake source models: 1. Comparisons with seismic catalogs, *J. geophys. Res.,* **116,** B08408, doi:10.1029/2010JB008131.

Weston, J., Ferreira, A.M.G. & Funning, G.J., 2012. Systematic comparisons of earthquake source models determined using InSAR and seismic data, *Tectonophysics,* **532–535,** 61–81.

Yagi, Y., 2004. Source rupture process of the 2003 Tokachi-oki earthquake determined by joint inversion of teleseismic body wave and strong ground motion data, *Earth Planets Space,* **56,** 311–316.

Downloaded from https://academic.oup.com/gji/article/195/3/1989/627339 by guest on 14 October 2021

Yamanaka, Y. & Kikuchi, M., 2003. Source process of the recurrent Tokachi-oki earthquake on september 26, 2003, inferred from teleseismic body waves, *Earth Planets Space,* **55,** e21–e24.

Zhang, Y., Chen, Y.-T. & Xu, L., 2012. Fast and robust inversion of earthquake source rupture process and its application to earthquake emergency response, *Earthq. Sci.,* **121,** doi:10.1007/s11589-012-0838-2.

Zobin, V.M., 1997. The rupture history of the Mw 8.0 Jalisco, Mexico, earthquake of 1995 October 9, *Geophys. J. Int.,* **130,** 220–228.

Zobin, V.M. & Levina, V.I., 2001. The rupture process of the Mw 7.8 Cape Kronotsly, Kamchatka earthquake of 5 December 1997 and its relationship to foreshocks and aftershocks, *Bull. seism. Soc. Am.,* **91**(6), 1619–1628.

SUPPORTING INFORMATION

Additional Supporting Information may be found in the online version of this article:

Figure S1. Teleseismic *P* and *SH* displacements, for an instantaneous point source located at 1 km depth.

Figure S2. Filtered teleseismic *P* and *SH* displacements, for a source located at 1 km depth.

Figure S3. Filtered teleseismic *P* and *SH* displacements, for a source located at 5 km depth.

Figure S4. Filtered teleseismic *P* and *SH* displacements, for a source located at 12 km depth.

Table S1. SCARDEC source parameters of the subduction earthquakes studied (strike—ϕ, dip—δ, rake—λ, moment magnitude—M_w, depth—Z) and their uncertainties for dip angle ($\Delta\delta$), depth (ΔZ) and moment magnitude (ΔM_w).

Table S2. Source duration values (T_d) obtained from studies in the literature and plotted as blue vertical lines for the earthquakes shown in Fig. 9 of the main manuscript (http://mnras.oxfordjournals.org/lookup/suppl/doi:10.1093/gjiras/ggt364/-/ DC1).

Please note: Oxford University Press is not responsible for the content or functionality of any supporting materials supplied by the authors. Any queries (other than missing material) should be directed to the corresponding author for the article.

Downloaded from https://academic.oup.com/gji/article/195/3/1989/627339 by guest on 14 October 2021